Tidal and spatial variability of flow speed and seismicity near the grounding zone of Beardmore Glacier, Antarctica

Jade COOLEY,[1,2] Paul WINBERRY,[1] Michelle KOUTNIK,[3] Howard CONWAY[3]

[1]Central Washington University, 400 E University Way, Ellensburg, WA 98926, USA
[2]University of Lethbridge, 4401 University Drive W, Lethbridge, AB T1K3M4, Canada.
E-mail: jade.cooley@uleth.ca
[3]University of Washington, Seattle, WA 98195, USA

ABSTRACT. GPS measurements of tidal modulation of ice flow and seismicity within the grounding zone of Beardmore Glacier show that tidally induced fluctuations of horizontal flow are largest near the grounding line and decrease downstream. Seismic activity is continuous, but peaks occur on falling and rising tides. Beamforming methods reveal that most seismic events originate from two distinct locations, one on the grid-north side of the grounding zone, and one on the grid-south side. The broad pattern of deformation generated as Beardmore Glacier merges with the Ross Ice Shelf results in net extension along the grid-north side of the grounding zone and net compression along the grid-south side. During falling tides, seismic activity peaks on both sides because of increased vertical flexure across the grounding line. During rising tides, seismic activity in the region of extension on the grid-north side is relatively low because the tidal influence on both horizontal strain rate and vertical flexure is small. On the grid-south side during rising tides, however, tidally induced horizontal strain rates promote increased seismicity in regions of long-term compressional flow paths. Our study highlights how concurrent geodetic and seismic measurements provide insight into grounding-zone mechanics and their influence on ice-shelf buttressing.

KEYWORDS: Antarctic glaciology, crevasses, glacier geophysics, ice-shelf tributary glaciers, seismology

INTRODUCTION

Antarctic ice sheet dynamics and sensitivity to climate change is of current interest because Antarctica's ice sheets could raise sea level by several meters over timescales of a few centuries (Joughin and Alley, 2011). Mass is discharged from the land-based part of Antarctica into ice shelves through glaciers and ice streams (e.g., Bentley and others, 1979; Bindschadler and others, 2011; Rignot and others, 2011). Buttressing from these ice shelves influences the rate at which mass is discharged from the ice sheet (e.g., DuPont and Alley, 2005; Fürst and others, 2016). Ocean tides induce stress perturbations that influence the vertical and horizontal motion of ice sheets near their marine margins (Padman and others, 2018). For example, flow speeds near the grounding zone of the Ross Ice Shelf have a predominately diurnal modulation that is similar to the dominant frequency of the Ross Sea tides (Anandakrishnan and others, 2003; Marsh and others, 2014). In contrast, near the grounding zone of Rutford Ice Stream on the Ronne Ice Shelf, where the ocean tides are predominantly semi-diurnal, the velocity response is strongest at fortnightly periods (Gudmundsson, 2007). Models used to explain this diverse behavior include non-linear basal sliding (Gudmundsson, 2007; Walker and others, 2013; Lipovsky and Dunham, 2017), hydrologic feedbacks (Rosier and others, 2016) and variable grounding throughout the tidal cycle (Robel and others, 2017).

Failure of near-surface crevasses is a dominant source of seismic activity near grounding zones (e.g., Barruol and others, 2013) and tidal modulation of velocity has the potential to induce seismic activity through influencing horizontal and vertical strain rates (Anandakrishnan and Alley, 1997). Previous work has shown that falling tides correspond with peak seismicity due to brittle failure and changes in strain rate. For example, on Bowdoin Glacier in Greenland, seismicity located a few kilometers upstream of the grounding zone also peaks on falling tides when extensional strain rates are highest (Podolskiy and others, 2016). Likewise, near-surface extensional stress near the grounding zone peaks during falling tides as a result of ice-shelf flexure (Barruol and others, 2013; Hulbe and others, 2016; Lombardi and others, 2016). Flow speed and seismicity are both sensitive to tidal perturbations, which makes it possible for simultaneous geodetic and seismic observations to elucidate the mechanical behavior of ice shelves near grounding zones.

Beardmore Glacier is a major outlet glacier that transports ice from the East Antarctic Ice Sheet through the Transantarctic Mountains into the Ross Ice Shelf. It drains a catchment area of ∼90 000 km^2 and reaches surface speeds of ∼400 m a^{-1} near the grounding zone (Rignot and others, 2011; Marsh and others, 2014). After Beardmore Glacier crosses the grounding zone, it is constrained by Mount Hope and Mount Kyffin (Fig. 1). Flow speed is modulated by the diurnal Ross Sea tides with peak velocities occurring during falling tides (Marsh and others, 2014). We combine geodetic and passive seismic observations that were collected simultaneously at the Beardmore Glacier grounding zone. Our geodetic observations show a spatially variable response of both vertical and horizontal motions in response
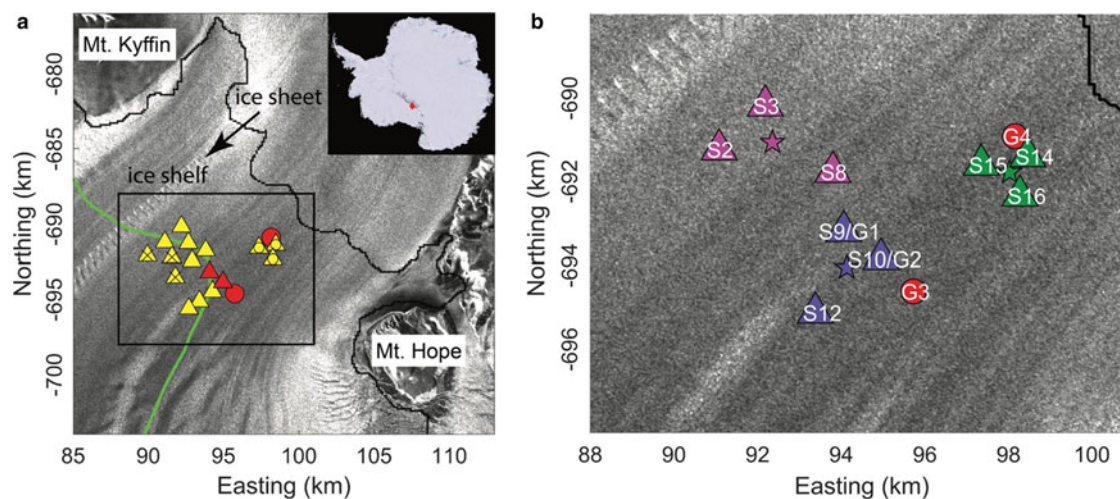
Fig. 1. Study area and station locations, black line is 2004 MOA grounding line (Haran and others, 2005). (a) Yellow triangles denote seismic-station locations and red circles denote GPS station locations. Stations marked with '×' were moved to locations marked with 'o' on 30 December. Two GPS stations were located near seismometers and their locations are combined as red triangles. Green line is the freely-floating boundary, or 'hydrostatic line' (Bindschadler and others, 2011). (b) Zoom of black box in (a), showing station locations in subarrays; seismometers denoted by 'S-'; GPS stations denoted by 'G-'. Array A1 (S2, S3, S8) is marked in pink, A2 (S9, S10, S12) in purple and A3 (S14, S15, S16) in green, with subarray centers marked by stars. Background image is the Radarsat Antarctic Mapping Project (RAMP) mosaic (Jezek and others, 2013).

to tidal forcing. Seismic activity also exhibits spatio-temporal variability that can be linked to tidal forcing of ice-shelf deformation.

DATA AND METHODS

Satellite-derived estimates of average velocity and longitudinal strain rate

To provide insight into the spatial structure of glacial behavior of the study region, we use a 2008–2009 annual velocity mosaic derived from the NASA Making Earth System Data Records for Use in Research Environments (MEaSURES) Interferometric Synthetic Aperature Radar (InSAR) data (Mouginot and others, 2017) (Fig. 2a). We use this velocity field to calculate the spatial distribution of longitudinal strain rates using the methods and codes of Alley and others (2018) (Fig. 2b). While a spatially continuous mosaic comprised of data from several epochs is available, artifacts from mosaicking proved it to be unsuitable for the calculation of strain rates in our study region. For calculation of strain, we use a length scale of 4 km (several ice thickness) that is a compromise between noise suppression and resolution. Additionally, prior to calculating strain rates, we remove all pixels for which velocity errors exceed 25 m a^{-1}.

GPS stations

We deployed a network of four GPS stations to monitor ice motion from 16 December 2013 to 7 January 2014. The network consisted of geodetic Trimble NetR9 receivers deployed 2–7 km downstream of the grounding line with each antenna affixed to a ~1.5 m metal conduit. Three stations were spaced ~1 km apart, in a line perpendicular to flow. The fourth station was located ~5 km upstream from this line (Fig. 1). Station positions were calculated using Precise Point Positioning methods (PPP; Zumberge and others, 1997) with the Natural Resource Canada's Canadian Spatial Reference System (CSRS-PPP) web

service. We examined both horizontal and vertical positions of these GPS stations over time to determine ice-shelf response to tidal velocity. Vertical motion is assumed to be due to tidal motion, and one GPS station was used to define the tidal range. Horizontal and vertical motions were calculated from the time series of positions smoothed using a 1 d low-pass Butterworth filter (Fig. 3).

Passive seismic observations and seismicity

At the same time period of the geodetic observations, we recorded seismic data from 13 passive seismic stations arranged in two geometries; the first operating for 14 d (16 December–30 December 2013) and the second operating for the remaining 8 d (31 December 2013–7 January 2014). The design and geometry of these arrays were constrained by the heavily crevassed surface of the study region. Trillium 120 Q/QA broadband seismometers connected to Trimble REFTEK data loggers sampling at 500 Hz were used for seismic data collection. The first set up was a tightly spaced rectangle ~6 km downstream from the grounding line, and the second set up was designed by moving three stations to an area ~5 km from the first rectangle, within 2 km of the grounding line (Fig. 1). Station spacing was ~1 km, which is the approximate ice thickness in this region (Fretwell and others, 2013).

Events recorded by the array typically had particle motions that indicate predominately Rayleigh surface waves. These characteristics are indicative of shallow sources, most likely generated by fracturing associated with near-surface crevasses (Deichmann and others, 2000; Mikesell and others, 2012). All data were bandpass filtered between 3 and 15 Hz, the dominant frequency range of seismic events recorded by the network. We then generate a catalogue of seismic events using the short-term average moving window divided by the long-term average moving window (Allen, 1978) (Fig. 4). We used a 2 s short-term and 120 s long-term average window. Event start times were selected when the short-term average divided by the
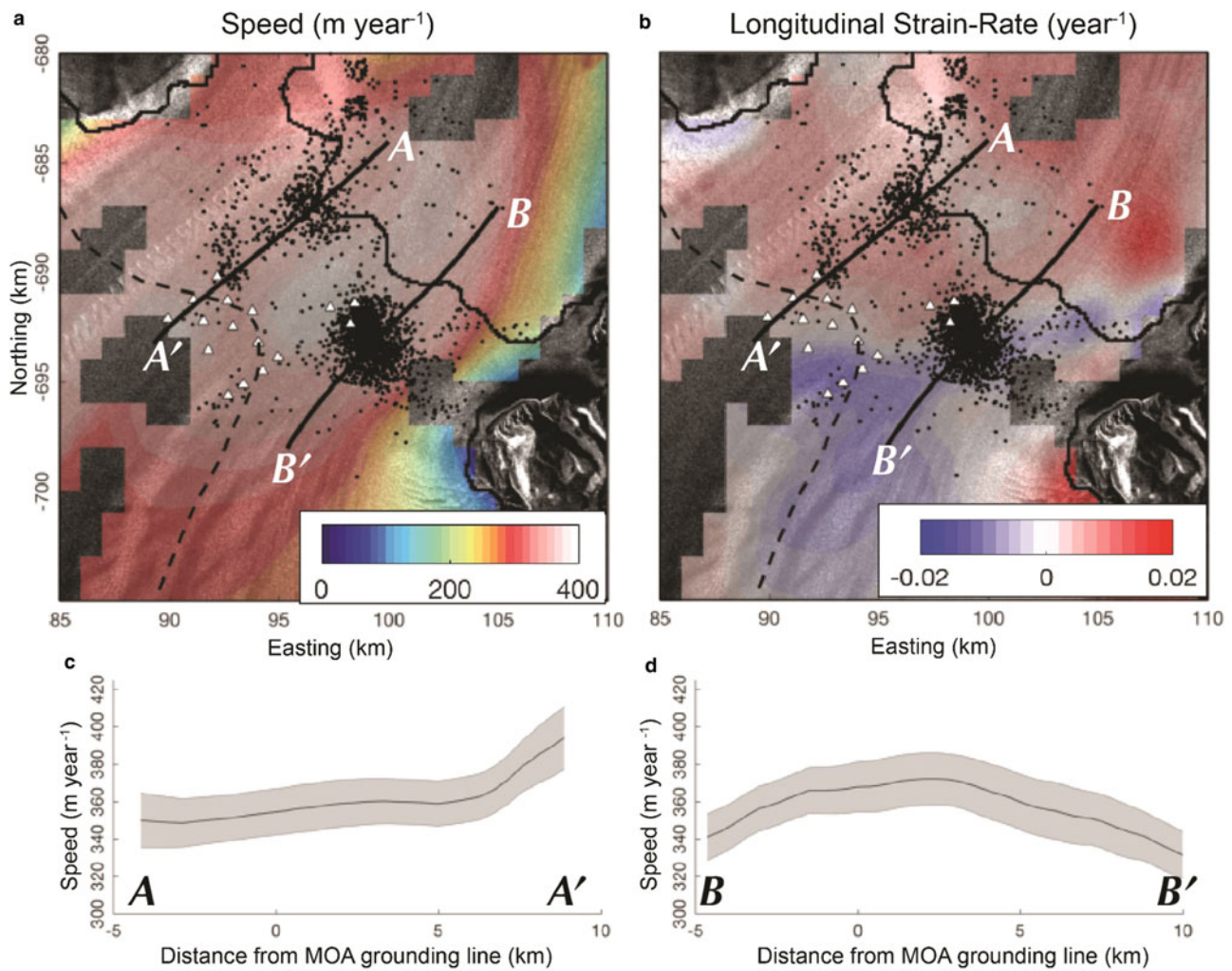
Fig. 2. (a) Ice speed from MEaSUREs (Mouginot and others, 2017). (b) Longitudinal strain rates (Alley and others, 2018). In both (a) and (b) well-located event epicenters are black dots, station locations are indicated by white transects, solid black line is 2004 MOA grounding line (Haran and others, 2005), dashed black line is ASAID hydrostatic line (Bindschadler and others, 2011). (c) and (d) show velocity transects along profiles in (a) and (b) with error from MEaSUREs in grey.

long-term average value exceeded 2.7, and event termination was defined to be when the ratio fell below 1.7. This high termination ratio minimizes counting multiple events occurring close together as a single event.

Event location

The lack of well-defined body waves for most events recorded by the network made it difficult to use a traditional seismic-event-location method, such as travel-time inversion
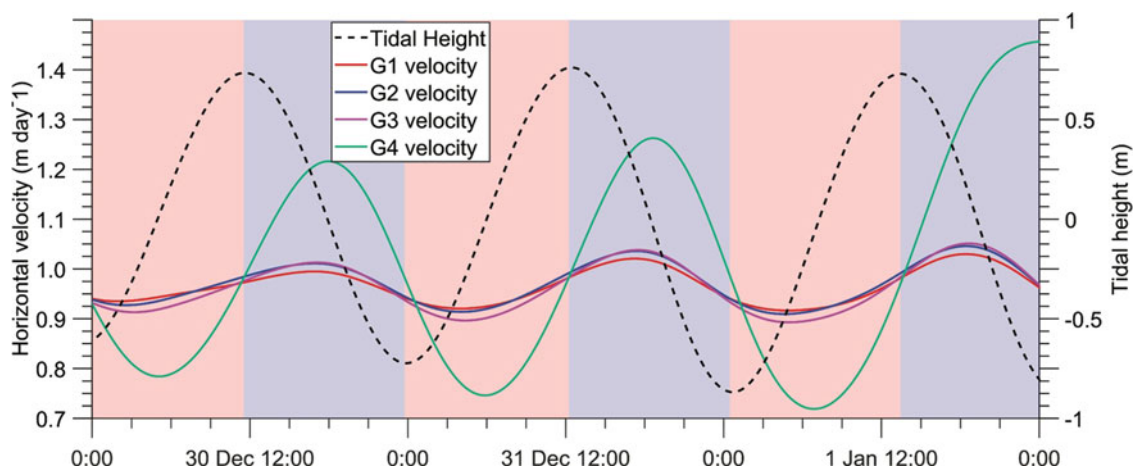
Fig. 3. Tidal variation in horizontal velocity measured by GPS stations. Tidal height is estimated from the vertical motion of station G2. Stations move slower during rising tides (shaded in red), and faster during falling tides (shaded in blue).
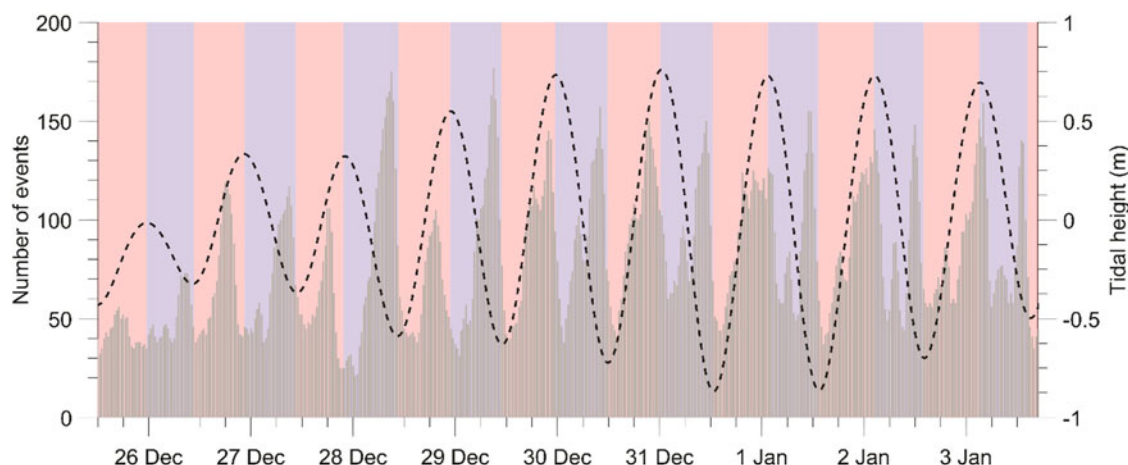
Fig. 4. Temporal pattern of seismicity, displayed in 30 min bins using a 3 h moving average. Rising tide is highlighted in red, falling tide in blue. Tidal height is estimated from the vertical motion of station G2.

of well-picked seismic phases (i.e., P and/or S waves). For a given event, however, waveforms exhibit similarity at neighboring stations (Figs 5a–c), which allows the use of the beam-forming method to estimate event locations (e.g., Rost and Thomas, 2002; Winberry and others, 2009; Richardson and others, 2010; Köhler and others, 2016). We estimated the source-direction and propagation speed of an incoming wave by calculating waveform coherency after iteratively shifting each waveform in the time domain by the time lags associated with a range of slowness values (slowness is defined as the inverse of velocity) and azimuths. If an event is well recorded by multiple arrays, the source location can

be estimated by the intersection of vectors that describe the azimuth estimate of each array. Our method is similar to that employed in solid-earth studies (e.g., Almendros and others, 2001).

For beamforming and event location, three subarrays consisting of three seismometers each were created. Subarray A1 consisted of seismometers S2, S3, S8; A2 of seismometers S9, S10, S12; and A3 of seismometers S14, S15, S16. The centers of these arrays are shown in Figure 1b. We ignore changes in our network geometry during the course of the deployment, as total motion (∼20 m) is small relative to the accuracy of our locations (several hundred meters). While events can be located using only two subarrays, events that originate along the trajectory connecting the two arrays will have azimuth estimates that are parallel to sub-parallel, leading to poor location estimates. Thus, we restrict the beamforming analysis to the period from 31 December 2013 to 7 January 2014 when sites S14–S16 were active. Coherence of the shifted waveforms was measured using the smoothed energy envelope function (0.5 s) of each waveform (Fig. 5).

Subsequent to beamforming for each subarray, a probabilistic estimate of the source location is made that takes into account conservative error estimates in azimuth (±20°). We first construct wedges that reflect the azimuthal probability distributions for each subarray (Figs 6a–c). A value of 1 is assigned along the estimated azimuth with values decreasing linearly to 0 as azimuths approach ±20° of the estimated azimuth. The azimuthal probability estimate of each subarray is then averaged at each gridpoint to create a spatial-source probability (Fig. 6d). When all three wedges overlap and a geographic point has a probability value close to one, the location is a possible source for the event.

Locating events precisely can be hampered by several factors, such as low signal-to-noise ratios, two events occurring very close in time relative to their duration or spatial variations in seismic wave speed. In addition, for events that originate from outside the network, the wedges that define the azimuthal probability estimate for each subarray become increasingly parallel, and at a certain distance, no minimum will exist in the spatial source probability. A resolution test indicates that this transition occurs ∼10 km from the center of the network (Cooley, 2017). We discard events with poor locations by imposing two conditions: (i) ensuring the spatial-source probability wedges from all
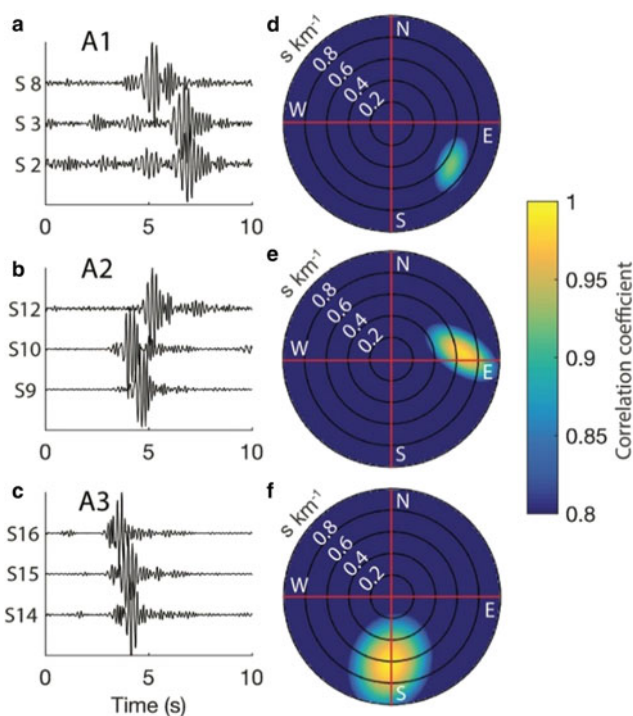

Fig. 5. Example of one seismic event (# 20 032 on 2 January 2014 at 2:08 pm, near the end of a rising tide) and the corresponding beamforming result. (a–c) Normalized bandpass filtered waveforms as they arrived at each station in the subarray. (d–f) Probability maps from searching through azimuths for all discrete values of a range of slownesses.
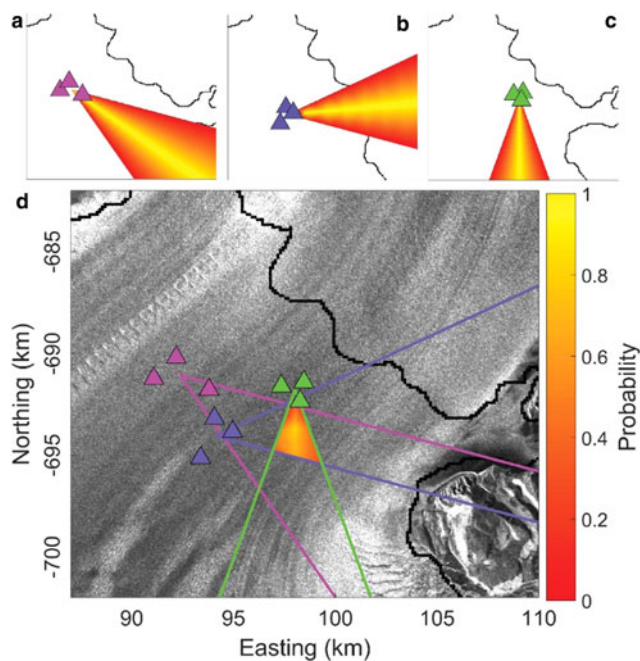
Fig. 6. Well-located event # 20 032 shown in Figure 5. Spatial probability distribution wedges for azimuth at arrays (a) A1 (pink), (b) A2 (purple) and (c) A3 (green). (d) Spatial source probability with outlines of wedges that define azimuth estimate ±20° for each subarray.

three subarrays overlap and (ii) excluding all events with the origin more than 10 km from the center of the network. To satisfy the first condition, we require that the averaged maximum of spatial source probability exceeds 0.67. Events that satisfy both conditions are considered well-located, and used for further investigation in this study.

RESULTS

Spatial structure of ice motion

The spatial structure of velocity and strain rate show that within a few kilometers downstream of the grounding zone, the ice-shelf can be divided into distinct regions: an extensional regime for ice exiting the grid-north side of the glacier, and a zone of net compression for ice exiting the grid-south side of the glacier (Fig. 2). There is no indication of pinning points in this region, which implies this region of compression arises from the redirection of flow as the glacier merges with the Ross Ice Shelf (LeDoux and others, 2017).

GPS observations of ice motion

As previously observed on the Ross Ice Shelf, all sites exhibit tidal modulation of their flow speed (Anandakrishnan and others, 2003; Marsh and others, 2013). While all GPS stations were deployed on the ice shelf, the observed vertical motion associated with the ocean tides varies according to proximity to the grounding zone. The smallest vertical range of ~1 m was observed at G4, while the downstream sites G1, G2 and G3 display larger vertical range (~1.8 m). This larger range is within a few centimeters of the modeled tidal ranges in the region for this time period (Padman and others, 2002). Annual horizontal velocities of the three downstream locations are ~348 m a^{-1}, while the

upstream site G4 moves at a slightly faster rate of 355 m a^{-1}, consistent with the long-term net compression (Fig. 2). We observe a slight phase difference in the modulation of flow speeds, with G4 reaching its highest and lowest velocity slightly later than stations farther downstream. Unlike previous surveys, our network displays less tidal modulation of the mean flow speed at the downstream locations (~5%) relative to upstream location (~20%).

Seismic event analysis

Event characteristics and timing

Events recorded by the network were typical of short duration (~3 s) with magnitudes between −2 and 0. We detected 24 028 events over the 23 d of 16 December 2013–7 January 2014, detecting 44 events per hour on average. Seismicity rate is not constant, however, but shows variations that correlate with the Ross Sea tides. At daily timescales, peaks in seismic activity are observed during both falling and rising tides (Fig. 4), while at the fortnightly timescale, neap tides (25–27 December) result in lower rates of seismic activity relative to the spring tides (30 December 2013–1 January 2014).

Event locations

Of the 8028 events detected during the 8 d period when all three subarrays were operating (31 December 2013–7 January 2014), approximately one-quarter of the events (2304) were well-located. We expect these event locations are representative of the entire event catalogue, as the events from this period have a similar tidally modulated pattern. Although events are located throughout the study area, there are two regions of more concentrated seismicity, one on the grid-north side of the region and one on the grid-south side. The seismicity in the grid-north part of the study area spans the grounding line and appears to be predominately associated with a train of crevasses that initially forms from an icefall within 5 km of the grounding zone (located at ~98–682 km). Seismicity on the south side of the region is concentrated downstream from the grounding line and is approximately centered over the transition between extensional and compressional flow regime observed on in the strain-rate maps (100–694 km) (Fig. 2b). Additionally, the temporal pattern of seismicity is distinct between the grid-north side and grid-south side of the study region. While a relatively low level of seismicity is always present (Fig. 4), seismicity on the north side of the study region peaks only during the falling tide (Fig. 7a). In contrast, seismic activity on the south side of the region has elevated the rates on both the falling and rising tides (Fig. 7b).

DISCUSSION

Tidal modulation of ice motion

At each of our GPS locations, peak horizontal velocities occur on the falling tide, with the magnitude of velocity fluctuations scaling with the daily tidal amplitude (Fig. 3). However, unlike other studies of tidally modulated ice-shelf flow (e.g., Brunt and others, 2010; Makinson and others, 2012), we observe decreased horizontal velocity modulation at our three downstream locations (G1, G2, G3) compared with the one upstream location (G4). The physical mechanisms that control both the phasing and
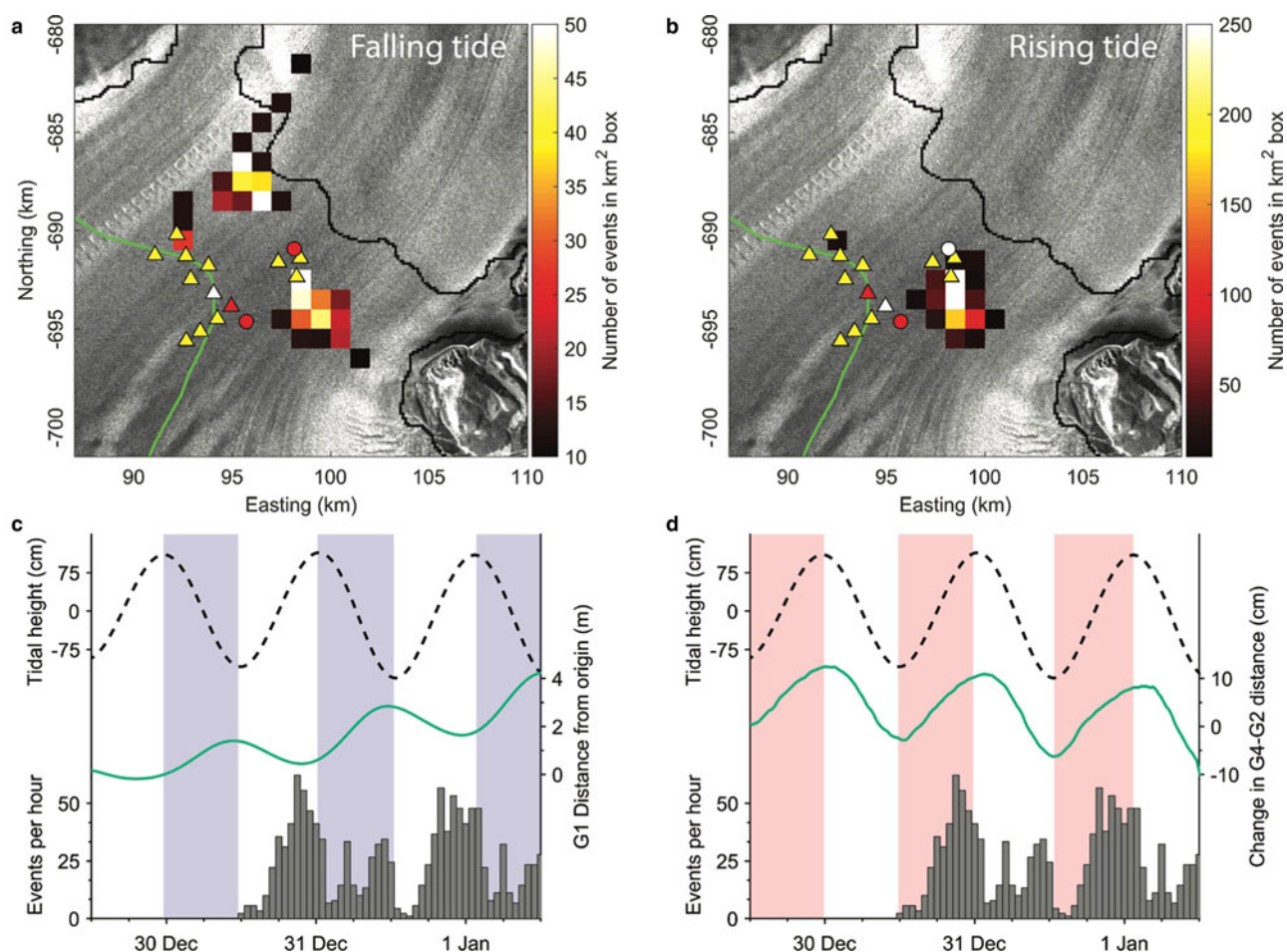
Fig. 7. Locations of events occurring during (a) falling tide and (b) rising tide. Boxes with less than ten events are not pictured. For (c) and (d) histograms of well-located events in grey (no well-located events on 30 December as A3 was not in place), black dashed line is tidal height (from G2), falling tide shaded in blue and rising tide shaded in red. (c) Line in green is the change in location of station G1, the white triangle in (a). The speed of G1 is tidally modulated, and the station moves slowly downstream, ~4 m over the 4 d pictured. (d) Line in green is horizontal distance between stations G2 and G4, the white triangle and circle respectively in (b).

magnitude of tidally modulated flow remain an active area of research (e.g., Robel and other, 2017). Tidal perturbations to the force budget are often small (a few kPa), and the magnitude of the velocity modulation is highly dependent on the tidally modulated force budget.

As ice crosses the Beardmore Glacier grounding line and merges with the Ross Ice Shelf, it must turn direction. This results in the zone of convergence observed along flow paths exiting the grid-south side of the glacier (Fig. 2b). Our GPS observations are concentrated near this region of net compression. Thus, the smaller magnitude of velocity modulation at the downstream sites (G1, G2, G3) relative to the upstream site (G4) is likely the result of increased buttressing in this portion of the ice-shelf, minimizing the influence of tidal perturbations on the flow field. A consequence of this behavior is that while the area on the grid-south side of the study area is a region of net compression, this region oscillates between horizontal extension and compression on daily timescales. At this location, horizontal extension occurs on rising tides as the velocity of locations closer to the grounding zone (such as G4) drops below that of the downstream locations (such as G1, G2, G3) (Fig. 3). This can be seen in the motion between stations G2 and G4, which move farther apart during rising tide (Fig. 7d).

Tidal modulation of seismicity

Elevated rates of fracture-related seismicity correspond to time periods of enhanced extensional strain rates. Near grounding zones, two main processes modulate strain rates on tidal timescales. Vertical flexure across the transition from a fully grounded ice sheet to a fully floating ice-shelf results in peak rates of extensional strain (e.g., Vaughan, 1994), and thus elevated rates of seismicity during the falling tide (Hulbe and others, 2016). The second dominant process is tidal modulation of horizontal flow speeds (e.g., Anandakrishnan and others, 2003), such as those observed in the Beardmore Glacier grounding zone.

Both mechanisms modulate the seismicity near the grounding zone of the Beardmore Glacier. However, there is a distinct temporal pattern in tidally modulated strain rates for the grid-north and grid-south portions of the region; this is illustrated in Figure 8. Average flow speeds increase monotonically for ice exiting the grid-north side of the glacier (Figs 2a and c), a characteristic that most likely indicates that peak horizontal strain rates will occur on the falling tide (Fig. 7c), similar to regions with simpler grounding-zone geometries (e.g., Barruol and others, 2013; Podolskiy and others, 2016). Thus, on the grid-north side of the glacier, extensional strain rates from both flexure and
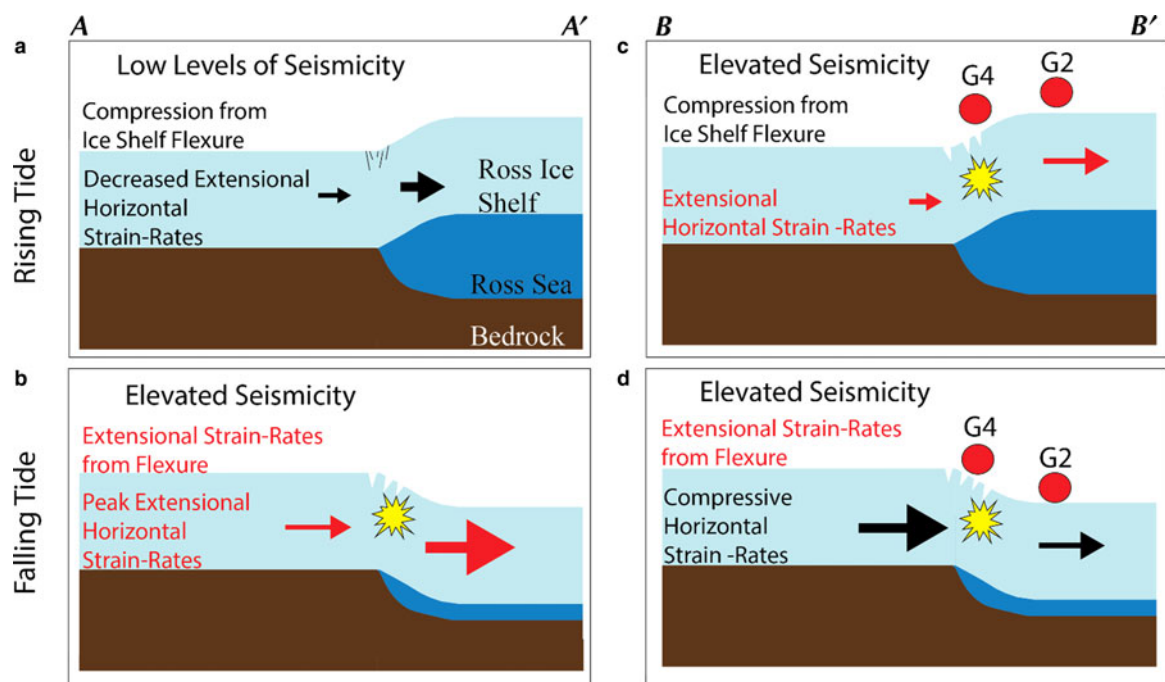
Fig. 8. Schematic of how the two main mechanisms influencing seismicity near grounding zones, vertical ice-shelf flexure and variable horizontal strain rates, vary during the tidal cycle for the two transects shown in Figure 2a and b. The vertical direction is exaggerated for clarity. Processes promoting increased levels of seismicity are in red, those promoting decreased levels of seismicity are in black. Explanation in section 'Tidal modulation of seismicity'.

horizontal velocity perturbations will promote lower levels of seismicity during rising tides (Fig. 8a), while the opposite is the case during falling tides (Figs 7 and 8b). In contrast, for the grid-south side of the study area, peaks in seismic activity are observed during both rising and falling tides (Figs 7a and b). The drop in ice flow speed near this section of the Beardmore grounding zone, relative to regions of ice-shelf a few kilometers downstream, results in peak horizontal strain rates during the rising tide, promoting increased seismic activity (Figs 7d and 8c). The opposite occurs on the falling tide as horizontal strain rates will tend to suppress seismic activity while positive strain rates drive flexure of the ice-shelf (Fig. 8d). Thus, the differing tidal modulation of seismic activity reflects the variable modulation of glacier flow due to the geometry of the study region.

CONCLUSIONS

Structural features that influence rift and stability of large ice shelves often originate from grounding zones (e.g., LeDoux and others, 2017). Our work highlights how observations of seismic activity near the grounding zone can be used to constrain the relationship between compression/extension of the ice-shelf due to tides and due to crevasse formation and propagation. The change in ice-flow trajectory as the Beardmore Glacier exits onto the Ross Ice Shelf makes it unique compared with outlet glaciers with small or non-existent ice shelves. The spatial variation in tidally modulated flow speed provides physical mechanisms to understand the links between the spatio-temporal pattern of strain rates and observed seismicity.

In addition to these findings, we present the successful application of the beamforming method for locating the epicenters of seismic events related to ice sheet motion. Our study area has two distinct regions of seismic activity that display unique temporal patterns. Investigating this reveals the complex interplay between glacier flow in the grounding zone, buttressing from the ice-shelf and tidal interactions. Future cryoseismic or geodetic studies could focus on the extension zone of the Beardmore Glacier, or on other glaciers with similarly complex grounding-zone flow. Simultaneous seismic and geodetic studies of grounding-zone deformation have the potential to provide information about the ice-shelf structure that regulates seismic activity, which will lead to improved understanding of ice-shelf stability.

REFERENCES

Allen RV (1978) Automatic earthquake recognition and timing from single traces. *Bull. Seismol. Soc. Am.*, **68**(5), 1521–1532

Alley KE and 5 others (2018) Continent-wide estimates of Antarctic strain rates from Landsat 8-derived velocity grids. *J. Glaciol.*, **64** (244), 321–332

Almendros J, Chouet B and Dawson P (2001) Spatial extent of a hydrothermal system at Kilauea Volcano, Hawaii, determined from array analyses of shallow long-period seismicity. 2. Results.

J. Geophys. Res., **106**(B7), 13581–13597 (doi: 10.1029/2001JB000309)

Anandakrishnan S and Alley RB (1997) Tidal forcing of basal seismicity of ice stream C, West Antarctica, observed far inland. *J. Geophys. Res.*, **102**(B7), 15183–15196 (doi: 10.1029/97JB01073)

Anandakrishnan S, Voigt DE, Alley RB and King MA (2003) Ice stream D flow speed is strongly modulated by the tide beneath the Ross Ice Shelf. *Geophys. Res. Lett.*, **30**(7), 1361 (doi: 10.1029/2002GL016329)

Barruol G and 5 others (2013) Tide-induced microseismicity in the Mertz glacier grounding area, East Antarctica. *Geophys. Res. Lett.*, **40**(20), 5412–5416 (doi: 10.1002/2013GL057814)

Bentley CR (1979) Ice-thickness patterns and the dynamics of the Ross Ice Shelf, Antarctica. *J. Glaciol.*, **24**(90), 287–294

Bindschadler R and 17 others (2011) Getting around Antarctica: new high-resolution mappings of the grounded and freely-floating boundaries of the Antarctic ice sheet created for the International Polar Year. *Cryosphere*, **5**, 569–588 (doi: 10.5194/tc-5-569-2011)

Brunt KM, King MA, Fricker HA and MacAyeal DR (2010) Flow of the Ross Ice Shelf, Antarctica, is modulated by the ocean tide. *J. Glaciol.*, **56**(195), 157–161 (doi: 10.3189/002214310791190875)

Cooley J (2017) Tidal and structural controls on seismic events near the grounding line at Beardmore Glacier, Antarctica. MSc Thesis: Central Washington University, 43 pp

Deichmann N and 5 others (2000) Evidence for deep icequakes in an Alpine glacier. *Ann. Glaciol.*, **31**, 85–90 (doi: 10.3189/172756400781820462)

Dupont TK and Alley RB (2005) Assessment of the importance of ice-shelf buttressing to ice-sheet flow. *Geophys. Res. Lett.*, **32**(4), L04503 (doi: 10.1029/2004GL022024)

Fretwell P and 59 others (2013) Bedmap2: improved ice bed, surface and thickness datasets for Antarctica. *Cryosphere*, **7**, 375–393 (doi: 10.5194/tc-7-375-2013)

Fürst JJ and 6 others (2016) The safety band of Antarctic ice shelves. *Nat. Clim. Change*, **6**(5), 479–482 (doi: 10.1038/nclimate2912)

Gudmundsson GH (2007) Tides and the flow of Rutford Ice Stream, West Antarctica. *J. Geophys. Res*, **112**(F4), F04007 (doi: 10.1029/2006JF000731)

Haran T, Bohlander J, Scambos T, Painter T and Fahnestock M (2005) updated 2013. *MODIS mosaic of Antarctica 2003–2004 (MOA2004) Image Map*. National Snow and Ice Data Center, Boulder, Colorado USA, http://dx.doi.org/10.7265/N5ZK5DM5

Hulbe CL and 5 others (2016) Tidal bending and strand cracks at the Kamb Ice Stream grounding line, West Antarctica. *J. Glaciol.*, **62**(235), 816–824 (doi: 10.1017/jog.2016.74)

Jezek KC, Curlander JC, Carsey F, Wales C and Barry RG (2013) *RAMP AMM-1 SAR Image Mosaic of Antarctica, Version 2*. NSIDC: National Snow and Ice Data Center, Boulder, Colorado, USA (doi: 10.5067/8AF4ZRPULS4H)

Joughin I and Alley RB (2011) Stability of the West Antarctic ice sheet in a warming world. *Nat. Geosci.*, **4**, 506–513 (doi: 10.1038/NGEO1194)

Köhler A and 5 others (2016) A 15 year record of frontal glacier ablation rates estimated from seismic data. *Geophys. Res. Lett.*, **43**(23), 12155–12164 (doi: 10.1002/2016GL070589)

LeDoux CM, Hulbe CL, Forbes MP, Scambos TA and Alley K (2017) Structural provinces of the Ross Ice Shelf, Antarctica. *Ann. Glaciol.*, **58**(75), 88–98 (doi: 10.1017/aog.2017.24)

Lipovsky BP and Dunham EM (2017) Slow-slip events on the Whillans Ice Plain, Antarctica, described using rate-and-state friction as an ice stream sliding law. *J. Geophys. Res. Earth Surf.*, **122**(4), 973–1003 (doi: 10.1002/2016JF004183)

Lombardi D and 5 others (2016) Bimodal pattern of seismicity detected at the ocean margin of an Antarctic ice shelf. *Geophys. J. Int.*, **206**(2), 1375–1381 (doi: 10.1093/gji/ggw214)

Makinson K, King MA, Nicholls KW and Gudmundsson GH (2012) Diurnal and semidiurnal tide-induced lateral movement of Ronne Ice Shelf, Antarctica. *Geophys. Res. Lett.*, **39**(1), L10501 (doi: 10.1029/2012GL051636)

Marsh OJ, Rack W, Floricioiu D, Golledge NR and Lawson W (2013) Tidally induced velocity variations of the Beardmore Glacier, Antarctica, and their representation in satellite measurements of ice velocity. *Cryosphere*, **7**, 1375–1384 (doi: 10.5194/tc-7-1375-2013)

Marsh OJ, Rack W, Golledge NR, Lawson W and Floricioiu D (2014) Grounding-zone ice thickness from InSAR: inverse modelling of tidal elastic bending. *J. Glaciol.*, **60**(221), 526–536 (doi: 10.3189/2014JoG13J033)

Mikesell TD and 5 others (2012) Monitoring glacier surface seismicity in time and space using Rayleigh waves. *J. Geophys. Res*, **117**(F2), F02020 (doi: 10.1029/2011JF002259)

Mouginot J, Rignot E, Scheuchl B and Millan R (2017) Comprehensive Annual Ice Sheet Velocity Mapping Using Landsat-8, Sentinel-1, and RADARSAT-2 Data, *Remote Sensing*. 9. Art. #364. https://doi.org/10.3390/rs9040364

Padman L, Fricker HA, Coleman R, Howard S and Erofeeva L (2002) A new tide model for the Antarctic ice shelves and seas. *Ann. Glaciol.*, **34**, 247–225 (doi: 10.3189/172756402781817752)

Padman L, Siegfried MR and Fricker HA (2018) Ocean tide influences on the Antarctic and Greenland Ice Sheets. *Rev. Geophys.*, **56**(1), 142–184 (doi: 10.1002/2016RG000546)

Podolskiy EA and 7 others (2016) Tide-modulated ice flow variations drive seismicity near the calving front of Bowdoin Glacier, Greenland. *Geophys. Res. Lett.*, **43**(5), 2036–2044 (doi: 10.1002/2016GL067743)

Richardson JP, Waite GP, FitzGerald KA and Pennington WD (2010) Characteristics of seismic and acoustic signals produced by calving, Bering Glacier, Alaska. *Geophys. Res. Lett.*, **37**(3), L03503 (doi: 10.1029/2009GL041113)

Rignot E, Mouginot J and Scheuchl B (2011) Ice flow of the Antarctic ice sheet. *Science*, **333**(6048), 1427–1430 (doi: 10.1126/science.1208336)

Robel AA, Tsai VC, Minchew B and Simons M (2017) Tidal modulation of ice shelf buttressing stresses. *Ann. Glaciol.*, **58**(74), 12–20 (doi: 10.1017/aog.2017.22)

Rosier SHR and Gudmundsson GH (2016) Tidal controls on the flow of ice streams. *Geophys. Res. Lett.*, **43**(9), 4433–4440 (doi: 10.1002/2016GL068220)

Rost S and Thomas C (2002) Array seismology: methods and applications. *Rev. Geophys.*, **40**(3), 2–1–2-27 (doi: 10.1029/2000RG0001002002)

Vaughan DG (1994) Investigating tidal flexure on an ice shelf using kinematic GPS. *Ann. Glaciol.*, **20**, 372–376

Walker RT and 5 others (2013) Ice-shelf tidal flexure and subglacial pressure variations. *Earth Planet. Sci. Lett.*, **361**, 422–428 (doi: 10.1016/j.epsl.2012.11.008)

Winberry JP, Anandakrishnan S and Alley RB (2009) Seismic observations of transient subglacial water-flow beneath MacAyeal Ice Stream, West Antarctica. *Geophys. Res. Lett.*, **36**(11), L11502 (doi: 10.1029/2009GL037730)

Zumberge JF, Heftin MB, Jefferson DC, Watkins MM and Webb FH (1997) Precise point positioning for the efficient and robust analysis of GPS data from large networks. *J. Geophys. Res.*, **102**(B3), 5005–5017 (doi: 10.1029/96JB03860)